Permeability impairment of a limestone reservoir triggered by heterogeneous dissolution and particles migration during CO2-rich injection

Papa Ousmane Mangane, Philippe Gouze, Linda Luquot

▶ **To cite this version:**

Papa Ousmane Mangane, Philippe Gouze, Linda Luquot. Permeability impairment of a limestone reservoir triggered by heterogeneous dissolution and particles migration during CO2-rich injection. Geophysical Research Letters, 2013, 40 (17), pp.4614-4619. 10.1002/grl.50595 . hal-00903585

HAL Id: hal-00903585
https://hal.science/hal-00903585

Submitted on 11 May 2021

HAL is a multi-disciplinary open access archive for the deposit and dissemination of scientific research documents, whether they are published or not. The documents may come from teaching and research institutions in France or abroad, or from public or private research centers.

L'archive ouverte pluridisciplinaire **HAL**, est destinée au dépôt et à la diffusion de documents scientifiques de niveau recherche, publiés ou non, émanant des établissements d'enseignement et de recherche français ou étrangers, des laboratoires publics ou privés.

Permeability impairment of a limestone reservoir triggered by heterogeneous dissolution and particles migration during CO_2-rich injection

Papa O. Mangane,[1] Philippe Gouze,[1] and Linda Luquot[1]

Received 24 May 2013; accepted 25 May 2013; published 13 September 2013.

[1] A CO_2-rich brine core-flood experiment in calcite limestone for conditions representative of underground storage ($P = 12$ MPa and $T = 100°C$) was performed in order to explore the dissolution mechanisms arising at moderate CO_2 partial pressure (0.3 MPa). An increase of the total porosity (φ_T) accompanied by a persistent permeability (k) decrease was measured. The mechanisms controlling this atypical anticorrelated $k - \varphi_T$ relationship were investigated from the analysis of high-resolution X-ray microtomography images of the sample acquired before and after the experiment. All the evidences converge to the conclusion that the ubiquitous decrease of permeability measured during the 44 h of dissolution is due to the clogging of a fraction of the macroporosity by microporous material triggered by the rearrangement of the detached undissolved particles. This mechanism results in the development of low permeability zones bridging the macroporosity. **Citation:** Mangane, P. O., P. Gouze, and L. Luquot (2013), Permeability impairment of a limestone reservoir triggered by heterogeneous dissolution and particles migration during CO_2-rich injection, *Geophys. Res. Lett.*, *40*, 4614–4619, doi:10.1002/grl.50595.

1. Introduction

[2] CO_2 geological storage (GCS) is considered as a way to decrease the carbon emissions of industrial processes (i.e., fossil fuel combustion). This is based upon nearly 40 years of oil industry experiments regarding CO_2 injection in reservoirs for enhancing the extraction of crude oil. Among other issues related, for instance, to caprock integrity, a main research subject concerns the change in reservoir flow dynamics (e.g., change in the rock permeability k) induced by the pore structure alteration during a CO_2 injection [*Hoefner and Fogler*, 1988; *Steefel and Lasaga*, 1990; *Golfier et al*., 2002]. The principal feature of CO_2 injection into geologic formation is the possible interactions between the fluid and the host rock, which trigger geochemical processes (dissolution/precipitation reactions) that depend on the rock composition and fabric, the brine composition, and the thermodynamic and hydrodynamic conditions. Results of reactive transport experiments, performed in reservoir rock sample [*Luquot and Gouze*, 2009; *Grigg and Svec*, 2003; *Qajar et al*., 2012] demonstrated that a rock structure modification can either impair or improve the permeability value k, depending on the fluid-rock thermodynamical disequilibrium and flow rate. Then, these mechanisms of pore structure alteration may largely control the injectivity, the pressure field dynamics, and the CO_2 spreading and consequently are crucial for developing predictive modeling tools and reliable risk assessment. Detailed laboratory-scale investigations of the geochemical processes controlling fluid-rock mass transfers critically contribute to understanding the key features of the system dynamics and forming the basis for the development of process-based models. However, application of reactive transport models to carbonate rock systems is especially challenging, because they are hampered by the heterogeneous distribution of pores and reactive minerals as well as uncertainties in the effective kinetic rates of carbonate minerals in CO_2-rich waters [*Carroll et al*., 2013].

[3] Carbonate reservoirs contain roughly half the world's oil and gas reserves. These reservoirs, when depleted, as well as deep-saline aquifers, are envisaged targets for long-term GCS. GCS consists of injecting supercritical more-or-less pure CO_2 into the formation porosity through boreholes. The progressive dissolution of CO_2 in the formation water (generally initially at thermodynamic equilibrium with the rock-forming minerals, e.g., calcite) leads to a decrease in pH and the dissolution of the carbonates species (see reviews in *Plummer et al*. [1978] and *Pokrovsky et al*. [2009]). In the vicinity of the injection well, where disequilibrium is maximal, dissolution processes will lead to an increase in porosity and permeability [e.g., *Egermann et al*., 2005]. For instance, *Luquot and Gouze* [2009] measured different porosity-permeability trends in the case of variable CO_2-enriched brine injection through the same oolitic carbonate used for this study. As a general rule, the permeability increase is triggered by the increase of the hydraulic radius, the decrease of the flow path tortuosity, and eventually the increase of the percolating network connectivity [*Gouze and Luquot*, 2011].

[4] However, few recent publications mention atypical porosity-permeability relationships with transient negative correlations attributed to particle displacement [*Qajar et al*., 2012]. The carbonate rocks are usually highly heterogeneous across all observation scales and formed by the aggregation of grains spanning a large range of sizes and degrees of induration as well as sparry calcite cement (or sparite). Cements dissolve faster than grains, and then grains become free particles because the solid matrix cohesion relies on the cement [*Noiriel et al*., 2009]. Accordingly, the origin of these flowing particles that can accumulate in the pore throats

[1]Géosciences, UMR 5243, Université de Montpellier 2, CNRS, Montpellier, France.

Corresponding author: P. O. Mangane, Université Montpellier 2, FR-34000 Montpellier, France. (mangane@gm.univ-montp2.fr)

©2013. American Geophysical Union. All Rights Reserved.
0094-8276/13/10.1002/grl.50595

may be linked to the intrinsic variability of the rock-forming grain sizes that triggered differential dissolution rates.

[5] Particles migration and deposition in porous media has long been known to have a critical effect on its hydraulic properties and consequently on production and injection wells performance [*Qajar et al*., 2012, *Richards*, 2010; *Mays and Hunt*, 2005; *Bennion et al*., 1995; *Sharma and Yortsos*, 1987]. Different models have been proposed to evaluate the effect of particle redistribution on permeability using the concept of plugging (pore throat and rough or tortuous channels) and nonplugging pathways (large cross-sectional channels) [e.g., *Gruesbeck and Collins*, 1982; *Civan and Nguyen*, 2005]. These models do not account for the particle detachment mechanism, for instance due to cement dissolution, but evaluate from macroscopic rules the particle displacement and accumulation. To the best of our knowledge, only indirect evidences, such as permeability impairment and particles displacement, have been published [*Noiriel et al*., 2004; *Qajar et al*., 2012].

[6] Another issue concerns the parameters that control the occurrence of negative porosity-permeability, while most laboratory experiments dealing with carbonate dissolution display positive correlations [*Smith et al*., 2012]. The pore structure heterogeneity is often cited as a critical parameter controlling the permeability change during dissolution [*Gouze and Luquot*, 2011; *Carroll et al*., 2013; *Smith et al*., 2012]. However, we envisage that the degree of undersaturation of the flowing solution should have a significant impact on the occurrence and the sustainability of the negative correlation between the porosity and the permeability during dissolution. In this letter, we first present the result of a flow-through experiment using the same rock and procedure as *Luquot and Gouze* [2009] but with a CO_2-rich brine displaying a lower partial pressure of CO_2 (P_{CO_2}); a negative correlation between the porosity and the permeability changes is measured. Then, X-ray tomography is used to investigate the redistribution of mass within the rock sample and to conclude on its effect on the permeability decrease.

2. Methods and Results

2.1. Experimental Procedure

[7] The experiment involved the injection of CO_2-enriched fluid through a cylindrical limestone core of 9 mm diameter (D) and 16 mm length (L). The reservoir rock is an oolitic calcite ($Ca_{0.99}Mg_{0.01}CO_3$) from the Mondeville formation of Middle Jurassic age (Paris Basin, France). The presence of Mg can be neglected in the mass balance calculation [*Luquot and Gouze*, 2009]. This sample is essentially composed of recrystallized ooliths, presenting a mean diameter of less than a few hundred micrometers. The rock displays two types of porosities that can be easily identified from standard microscope observations; the intergranular porosity and the intragranular porosity formed mainly by the oolitic rings (see Figure S1 in the supporting information). The total connected porosity of the sample before injection is 12.62%. This was measured by weighing the sample dry (w_{dry}), saturated (w_{sat}), and immersed (w_{imm}), with a precision balance of 1 mg accuracy and water prepared to be at equilibrium with the mineral: $\varphi = \frac{(w_{sat} - w_{dry})}{(w_{sat} - w_{imm})}$.

[8] The experiment was performed using a flow-through device engineered to simulate the conditions expected during CO_2 injection in deep reservoirs. Fluid pressure and temperature were set to $P = 12$ MPa and $T = 100°C$, respectively. The injected fluid is a synthetic pore fluid (brine) of composition corresponding to the thermodynamic equilibrium with the rock ($C_{Ca} = 1.09 \times 10^{-2} \pm 0.05 \times 10^{-2}$ mol L^{-1}, $C_{Mg} = 1.708 \times 10^{-4} \pm 0.08 \times 10^{-4}$ mol L^{-1}, $C_{Na} = 0.966 \pm 0.05$ mol L^{-1}, and $C_{Cl} = 0.988 \pm 0.05$ mol L^{-1}, pH = 7.55), then enriched in CO_2 with a partial pressure of 0.3 MPa. The fluid composition and pressure correspond to the conditions expected far away from the injection well, where the CO_2 concentration is low due to the CO_2 consumption by the dissolution processes occurring along the flow path. Dissolution is expected to be the prevailing mass transfer mechanism because of the low value of pH (pH = 3.9) and negative value of the saturation index for calcite ($\Omega_{cal}|_{in} = -3.72$).

[9] A complete description of the equipment is given in *Luquot and Gouze* [2009] and is summarized in Figure 1. The experiment was performed with a constant flow rate of $Q = 1$ mL min^{-1}.

2.2. Monitoring Changes in Porosity and Permeability

[10] The limestone permeability $k(t)$ during the experiment was calculated from the monitored pressure drop $\Delta P(t)$ across the rock sample, according to Darcy's law: $k(t) = \mu \times L \times Q \times (S \times \Delta P(t))^{-1}$, where L is the length of the sample, S is the cross-sectional area, and μ is the dynamic viscosity of the fluid.

[11] The outlet fluid was regularly sampled and analyzed for Ca concentrations using Inductively Coupled Plasma Atomic Emission Spectroscopy. The porosity change with time was calculated from mass balance between the inlet and the outlet chemical composition: $\partial\varphi(t)/\partial t = \upsilon Q \Delta C_{Ca}(t)/V$, where υ is the calcite molar volume (3.7×10^{-5} m^3 mol^{-1}), ΔC_{Ca} denotes the difference in calcium concentration between the outlet ($C_{Ca}|_{out}$) and the inlet ($C_{Ca}|_{in}$), and V is the volume of the sample (i.e., $V = \pi L D^2/4$). Accordingly, the porosity is

$$\varphi(t) = \varphi(0) + \int_{t'=0}^{t} \mathrm{d}t' \partial\varphi\left(t'\right)/\partial t' = \varphi(0) + \upsilon Q V^{-1} \int_{t'=0}^{t} \mathrm{d}t' \Delta C_{Ca}\left(t'\right), \quad (1)$$

where $\varphi(0)$ denotes the porosity before the experiment (i.e., 12.62%). The time-resolved porosity and permeability in the course of the flow-through experiment are given in Figures 2a and 2b, respectively. Porosity increased with time, whereas the permeability decreased. This enhancement of the porosity with time denotes the occurrence of dissolution processes as expected from the negative value of the saturation index of the inlet brine $\Omega_{cal}|_{in}$. The saturation index of the outlet fluid is also estimated negative ($\Omega_{cal}|_{out} = -3.69$). We note (Figure 2a) that the calcium concentration in the effluent $C_{Ca}|_{out}$ was higher than in the injected brine $C_{Ca}|_{in}$, which confirms the removal of calcium from the sample. Conversely, the values of $C_{Ca}|_{out}$ were much lower than the equilibrium value indicating that dissolution proceeds far from equilibrium.

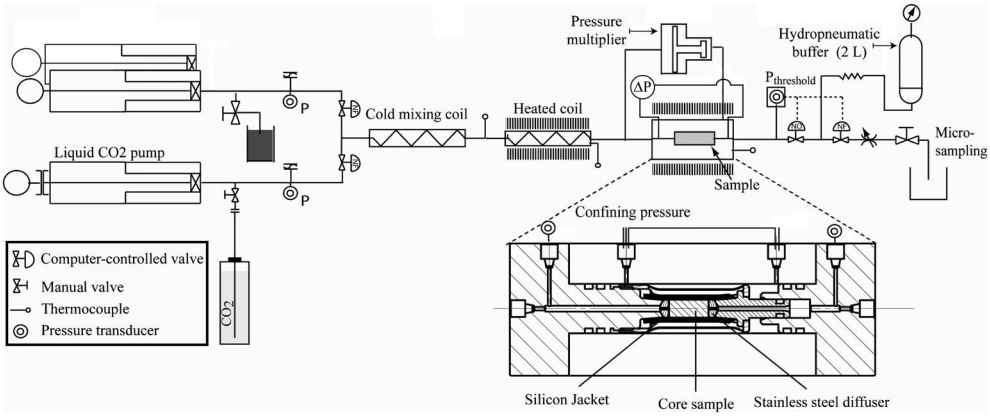

Figure 1. Diagram of the experimental setup. The ratio of the brine (room temperature) and liquid CO_2 (5°C) is controlled by computer-controlled piston pumps. The mixture is heated and injected into the core sample. The latter is surrounded by a silicon jacket and fitted inside the percolation cell where both axial and radial confining pressures are applied. The computer-controlled valves and the hydro-pneumatic back-pressure system force the desired pressure in the circuit with fluctuations less than 2%.

2.3. X-Ray Microtomography

[12] High-resolution X-ray microtomography (XRMT) of the sample was performed before and after the experiment, in order to investigate the changes in the microstructure triggered by the dissolution processes. XRMT images were acquired at the European Synchrotron Radiation Facility in Grenoble, France, using the ID19 beam line (http://www.esrf.eu/UsersAndScience/Experiments/Imaging/ID19/BeamlineDescription). The voxel volume of the images was $5.06^3\ \mu m^3$. The principle of XRMT is described in the supporting information (see Text S1).

2.3.1. Identification of the Different Types of Porosity

[13] A three-phase image segmentation algorithm, based on the growing phase method [*Spirkovska*, 1993], was used to determine the three distinguishable components of the rock: (1) the intergranular porosity formed by voxels of the lowest X-ray adsorption denoting void, (2) the microporous phase containing voxels encompassing calcite and pores of size smaller than the pixel size, and (3) the solid matrix phase, which presents the highest X-ray adsorption. The segmentation is a crucial data processing step because it determines the porosity and the geometry of the individualized phase interfaces. Usually, the segmentation is based on the X-ray adsorption histogram only, but this does not guarantee that the structure and the porosity are appropriately identified. Here the four input parameters required for the three-phase segmentation of the image acquired before the injection were sequentially optimized in order to minimize the difference between the measured total connected porosity and that computed from the segmented image. A similar approach was applied for the postdissolution image using the value of porosity given by equation (1).

[14] The total connected porosity is $\varphi_T = \xi_V + (\xi_\mu \times \varphi_\mu)$, where ξ_V denotes the volume fraction of the void phase or namely the macroporosity, and φ_μ and ξ_μ denote the intrinsic porosity and the volume fraction of the microporous phase, respectively. Accordingly, one can define the sample microporosity as $\varphi_m = \xi_\mu \times \varphi_\mu$. Since the gray-scale values corresponding to the solid matrix and void have been determined (noted θ_M and θ_v, respectively), the gray-scale value of a voxel belonging to the microporous phase ($\theta\mu$) is linearly related to the subresolution porosity φ_μ within that voxel: $\varphi_\mu = (\theta_M - \theta_\mu)/(\theta_M - \theta_v)$.

[15] The sample porosity φ_T computed from the XRMT images was 12.65% before the flow-through experiment, while the corresponding measured value $\varphi(0)$ was 12.62%. After the dissolution, the computed porosity was 13.90%,

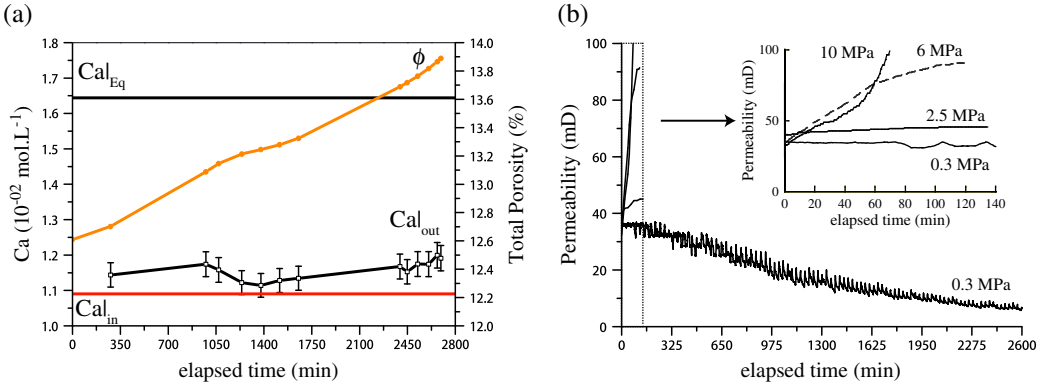

Figure 2. (a) Calcium concentration of the outlet fluid $C_{Ca}(t)|_{out}$ and sampled-average porosity $\varphi(t)$ versus time. (b) Permeability versus time $k(t)$ for the present study ($pCO_2 = 0.3$ MPa) together with the values reported in *Luquot and Gouze* [2009] for $P_{CO_2} = 10$, 6, and 2.5 MPa.

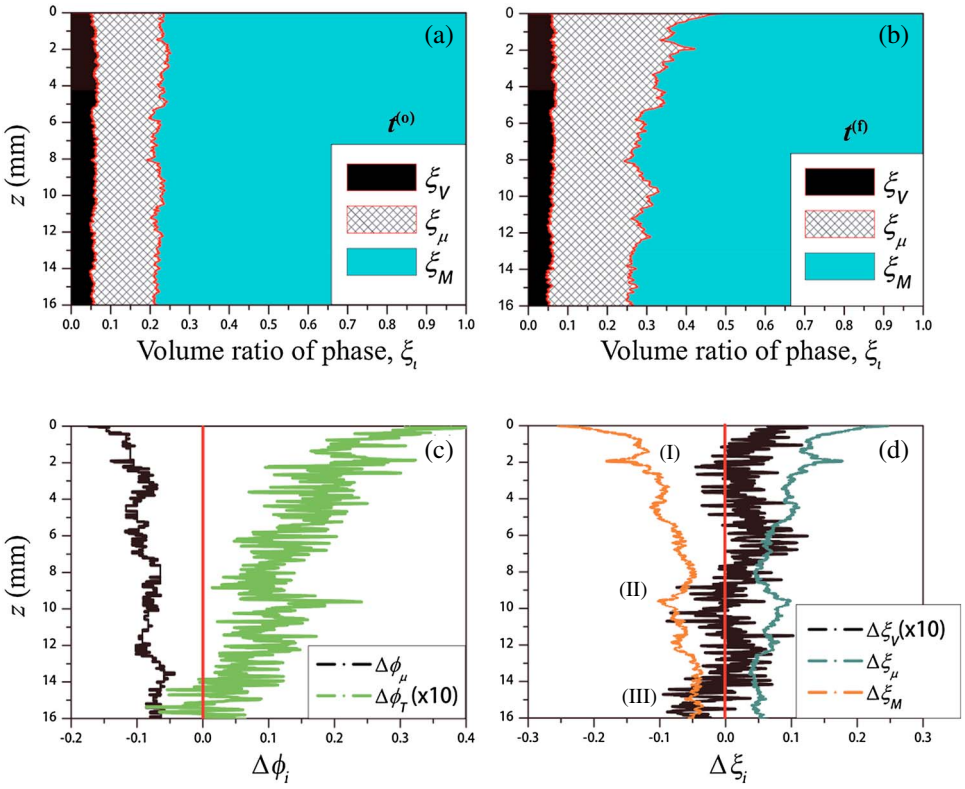

Figure 3. Volume fraction of the three identified phases constituting the rock versus the distance z from the injection (a) before ($t = t^{(0)}$) and (b) after ($t = t^{(f)}$) the dissolution experiment. Profiles of (c) the total porosity, $\Delta\varphi_T$, and the microporous phase intrinsic porosity, $\Delta\varphi_\mu$ and (d) volume ratio change $\Delta\xi_V$, $\Delta\xi_\mu$, $\Delta\xi_M$ ($z = 0$ denotes the sample inlet).

while $\varphi(f)$ was 13.89%. The relative increase of porosity due to the calcite dissolution during the experiment was then of about 10%.

[16] In the following discussion, the segmented images will be used to calculate the spatial distribution of the phase volume ratio and subsequently assess the mass redistribution along the flow path.

2.3.2. Phase Volume Fraction Changes

[17] The profiles (along the flow direction) of the volume fraction for each phase calculated before and after the experiment are reported in Figures 3a and 3b. The main features are the overall increase of the microporous phase ξ_μ ($\Delta\xi_\mu = \xi_\mu(t^{(f)}) - \xi_\mu(t^{(0)}) = 0.079$) while the volume fraction of the solid matrix phase ξ_M decreases ($\Delta\xi_M = -0.081$), with a minor increase in the macroporosity ($\Delta\xi_V = 0.002$). This indicates that the main process is the alteration of the solid matrix into a microporous phase by dissolution of the intergrain calcite cement. More instructive information can be retrieved from the profiles expressed in terms of $\Delta\varphi_T(z)$, $\Delta\varphi_\mu(z)$, $\Delta\xi_V(z)$, $\Delta\xi_\mu(z)$, and $\Delta\xi_M(z)$ (Figures 3c and 3d). The mass transfer appears to be higher at the inlet denoting a higher dissolution. This feature is evidently linked to the progressive decrease of the fluid disequilibrium while flowing deeper in the sample. The bulk porosity φ_T of the limestone core increases at all depths ($\Delta\varphi_T > 0$) along the flow direction, except at the bottom of the sample where it is significantly reduced, i.e., $\Delta\varphi_T < 0$ (Figure 3c). Obviously, a decrease of porosity cannot be explained by dissolution processes but rather indicates mass transfers of solid (particles) triggered by the fluid flow. Moreover, Figure 3d shows that $\Delta\xi_M(z)$ and $\Delta\xi_\mu(z)$ profiles are almost symmetric while $\Delta\xi_V(z)$ oscillates between positive and negative values with a value of the correlation length of about half that of the sample. The decrease of $\Delta\xi_V$ is about 6.6% in the vicinity of the outlet. We recall that the mass balance (equation (1)) is performed at the sample scale, so that no constraint is imposed for the redistribution of the phase within the sample. Another significant result is that the porosity of the microporous phase, φ_μ, is globally reduced ($\Delta\varphi_\mu(z) < 0$, Figure 3c), while its volume ratio is enhanced due to the matrix dissolution ($\Delta\xi_\mu(z) > 0$). Probably, this reduction of φ_μ is due to both the averaging of different stages of cement dissolution within the microporous volume and the local rearrangements of the freed grains. This apparent compaction (or densification) is slightly more pronounced in the vicinity of the sample inlet and does not correlate with $\Delta\xi_\mu$.

3. Discussion and Conclusions

[18] The permeability change in the course of CO_2 injection in carbonate reservoir is a major issue because of the high reactivity of these environments at low pH. The formation of preferential paths and the resulting permeability increase such as experimented by *Luquot and Gouze* [2009] (see Figure 2b), who investigated the mechanisms of dissolution at high pCO_2 expected in the vicinity of the injection well, are viewed as favoring both the pressure dissipation and the spreading and mixing of the CO_2. However, the present results of the core-flood experiment performed in the same conditions of dissolution but with lower pCO_2 showed significant clogging of the macropores and permeability decrease.

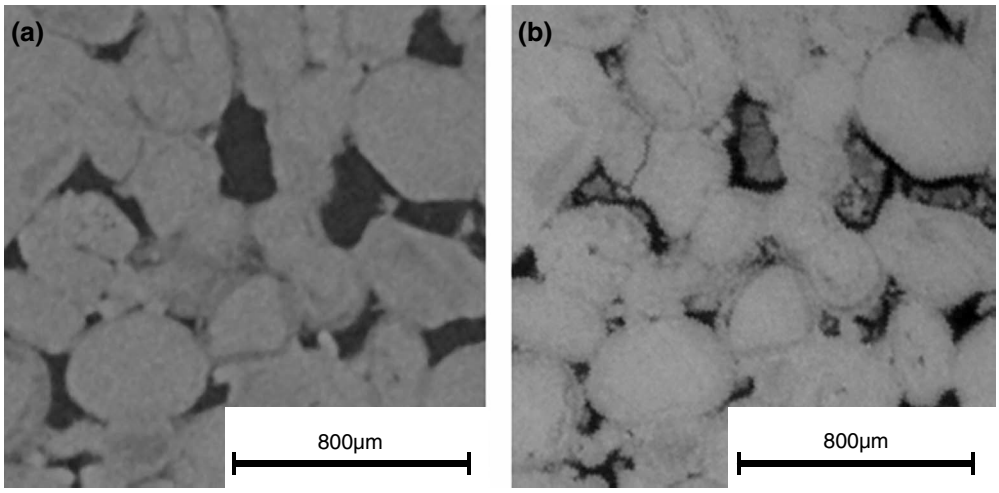

Figure 4. 2-D slice through 3-D XRMT image of the rock sample at $z = 15.2$ mm (a) before and (b) after the dissolution experiment displaying macropores filled with microporous material.

[19] The analysis of the XRMT images shows that the dominant mechanism is the dissolution of the microcrystalline cement triggering the decohesion of the rock matrix and then the formation of a microporous material (Figure 3d). This leads to the formation of a continuous layer of microporosity (see Figure S2 in the supporting information) at the interface between the macropores and the solid matrix phase, whereas both these phases were mostly in contact before the experiment. A cluster labeling algorithm [*Hoshen and Kopelman*, 1976] was used to determine if the different porosity phases (i.e., void, microporous, and "void + microporous") formed a spanning cluster from the inlet to the outlet. Both the void phase and the microporous phase displayed a spanning cluster before the injection. Conversely, only the microporous phase and the union of the void and the microporous phases were percolating after the experiment, i.e., the macroporosity did not form a spanning cluster anymore. Therefore, the permeability was closely controlled by the microporous phase at the end of the dissolution experiment. This observation cannot be explained by the exchange of volume from the matrix phase to the microporous phase only. Conversely, the spatial redistribution of a particle fraction forming the external layer of the microporous material is evidenced by the occurrence of negative values of $\Delta\xi_V$ that are observed around $z = 2$, $z = 9$, and $z = 15$ mm (noted I, II, and III in Figure 3d). A clear evidence of the displacement and accumulation of solid particles is given in Figure 4 that displays a 2-D slice through 3-D XRMT image of the rock sample in the vicinity of the outlet ($z = 15.2$ mm) where microporous material fills most of the macropores. At this location, both variations of the void phase fraction $\Delta\xi_V$ and of the total porosity $\Delta\varphi_T$ are negative. As the fluid sampling at the outlet was performed without filtering and the fluid samples were acidified before analysis, any particles dragged out from rock sample by the flow would strongly increase the calcium concentration of these fluid samples ($[\mathrm{Ca}|_{\mathrm{out}}]$). Consequently, the fact that the outlet fluid concentration remains close to the inlet concentration (Figure 2a) indicates that the mass of particles transported out of the rock sample is quite small. We speculate that the particle displacement takes place over short distances and that this traveling distance probably decreases with the distance to the inlet because the dissolution capacity of the fluid decreases from the inlet to the outlet.

[20] All the evidence converges to the conclusion that the ubiquitous decrease of permeability measured during the 44 h of dissolution was due to the clogging of a fraction of the macroporosity by microporous material (few µm-sized particles) triggered by the rearrangement of the detached undissolved grains (submicrometric to micrometric particles). This mechanism results in a noticeable increase of the permeability variability along the flow path. Specifically, the development of low permeability zones bridging the macroporosity will control the overall permeability by increasing the tortuosity of the connected path and decreasing the sample-scale effective hydraulic radius. However, it is not possible to establish how long this dissolution regime displaying permeability decrease will persist, because of the relatively short duration of the experiment. Comparing the results from this experiment to those presented by *Luquot and Gouze* [2009], we conjecture that the occurrence of permeability decrease due to particle accumulation depends on the capacity of the fluid to dissolve these particles over distances of the order of magnitude of half the throat-to-throat distances, i.e., about 200 to 400 µm at the beginning of the experiment.

[21] The implication in terms of injectivity is twofold. For constant pressure injection, the injected rate will be substantially decreased impairing the operation efficiency. Conversely, the increase of pore pressure produced in the case of constant rate injection may induce stress gradients possibly detrimental for the reservoir integrity.

[22] **Acknowledgments.** The authors thank the two anonymous reviewers for their insightful comments and suggestions. This work has been supported by the French National Research Center (CNRS) and the EU-funded project PANACEA (UE-7thFP - ENERGY 282900).

[23] The Editor thanks two anonymous reviewers for their assistance in evaluating this paper.

References

Bennion, D. B., F. B. Thomas, D. W. Bennion, and R. F. Bietz (1995), Mechanisms of formation damage and permeability impairment associated with the drilling, completion and production of low API gravity oil reservoirs, paper presented at SPE International Heavy Oil Symposium, Soc. of Pet. Eng., Calgary, Alberta, Canada.

Carroll, S., Y. Hao, M. Smith, and Y. Sholokhova (2013), Development of scaling parameters to describe CO_2–rock interactions within Weyburn-Midale carbonate flow units, *Int. J. Greenhouse Gas Control*, *16*(S1), S185–S193.

Civan, F., and V. Nguyen (2005), Modeling particle migration and deposition in porous media by parallel pathways with exchange, in *Handbook of Porous Media*, edited by K. Vafai, chap. 11, pp. 457–484, CRC Press, Boca Raton, Fla.

Egermann, P., B. Bazin, and O. Vizika (2005), An experimental investigation of reaction-transport phenomena during CO_2 injection, paper SPE 93674 presented at SPE Middle East Oil Show, Soc. of Pet. Eng., Manama, Bahrain.

Golfier, F., C. Zarcone, B. Bazin, R. Lenormand, D. Lasseux, and M. Quintard (2002), On the ability of a Darcy-scale model to capture wormhole formation during the dissolution of a porous medium, *J. Fluid Mech.*, *457*, 213–254.

Gouze, P., and L. Luquot (2011), X-ray microtomography characterization of porosity, permeability and reactive surface changes during dissolution, *J. Contam. Hydrol.*, *120*, 45–55.

Grigg, R. B., and R. K. Svec (2003), Co-injected CO_2-brine interactions with Indiana limestone, paper presented at the 2003 Symposium of the Society of Core Analysts, Pau, France.

Gruesbeck, C., and R. Collins (1982), Entrainment and deposition of fine particles in porous media, *SPEJ Soc. Pet. Eng. J.*, *22*(6), 847–856.

Hoefner, M., and H. S. Fogler (1988), Pore evolution and channel formation during flow and reaction in porous media, *AIChE J.*, *34*(1), 45–54.

Hoshen, J., and R. Kopelman (1976), Percolation and cluster distribution. I. Cluster multiple labeling technique and critical concentration algorithm, *Phys. Rev. B*, *14*(8), 3438.

Lasaga, A. C., (1981), Kinetics of geochemical processes, in *Kinetics of Geochemical Processes*, *Rev. Mineral.*, vol. 8, edited by A. C. Lasaga and R. J. Kirkpatrick, pp. 1–68, Mineralogical Society of America, Chantilly, Va.

Luquot, L., and P. Gouze (2009), Experimental determination of porosity and permeability changes induced by injection of CO_2 into carbonate rocks, *Chem. Geol.*, *265*(1), 148–159.

Mays, D. C., and J. R. Hunt (2005), Hydrodynamic aspects of particle clogging in porous media, *Environ. Sci. Technol.*, *39*(2), 577–584.

Noiriel, C., P. Gouze and D. Bernard (2004), Investigation of porosity and permeability in relation with microstructure changes during limestone dissolution, *Geophys. Res. Lett.*, *31*, L24603, doi:10.1029/2004GL021572.

Noiriel, C., L. Luquot, B. Madé, L. Raimbault, P. Gouze, and J. Van Der Lee (2009), Changes in reactive surface area during dissolution process: An experimental and modelling study, *Chemical Geol.*, *265*, 160–170.

Plummer, N., T. M. L. Wigley, and D. L. Parkhurst (1978), The kinetics of calcite dissolution in CO_2-water systems at 5 to 60°C and 0.0 to 1.0 atm CO_2, *Am. J. Sci.*, *278*, 179–216.

Pokrovsky, O. S., S. V. Golubev, J. Schott, and A. Castillo (2009), Calcite, dolomite and magnesite dissolution kinetics in aqueous solutions at acid to circumneutral pH, 25 to 150°C and 1 to 55 atm CO_2: New constraints on CO_2 sequestration in sedimentary basins, *Chem. Geol.*, *265*(1), 20–32.

Qajar, J., N. Francois, and C. Arns (2012), Micro-tomographic characterization of dissolution-induced local porosity changes including fines migration in carbonate rock, paper presented at SPE EOR Conference at Oil and Gas West Asia, Muscat, Oman, Soc. of Pet. Eng., 153216-MS.

Richards, T. (2010), Particle clogging in porous media, *SKB TR-10-22*, Swed. Nucl. Fuel and Waste Manage. Co., Stockholm.

Sharma, M. M., and Y. C. Yortsos (1987), Fines migration in porous media, *AIChE J.*, *33*(10), 1654–1662.

Smith, M. M., Y. Sholokhova, Y. Hao, and S. A. Carroll (2012), Evaporite caprock integrity: An experimental study of reactive mineralogy and pore-scale heterogeneity during brine-CO2 exposure, *Environ. Sci. Technol.*, *47*(1), 262–268.

Spirkovska, L. (1993), A summary of image segmentation techniques, *NASA Tech. Memo.*, *TM-104022*.

Steefel, C. I., and A. Lasaga (1990), Evolution of dissolution patterns, in *Chemical Modeling in Aqueous Systems II, ACS Symp. Ser.*, vo.l 416, pp. 212–225, Am. Chem. Soc., Washington, D.C.